



# Conceptual study on nucleation burst evolution in the convective boundary layer ? Part III: Physico-chemical characterization

O. Hellmuth

## ► To cite this version:

O. Hellmuth. Conceptual study on nucleation burst evolution in the convective boundary layer ? Part III: Physico-chemical characterization. Atmospheric Chemistry and Physics Discussions, 2005, 5 (6), pp.11517-11555. hal-00301920

HAL Id: hal-00301920

<https://hal.science/hal-00301920>

Submitted on 18 Jun 2008

**HAL** is a multi-disciplinary open access archive for the deposit and dissemination of scientific research documents, whether they are published or not. The documents may come from teaching and research institutions in France or abroad, or from public or private research centers.

L'archive ouverte pluridisciplinaire **HAL**, est destinée au dépôt et à la diffusion de documents scientifiques de niveau recherche, publiés ou non, émanant des établissements d'enseignement et de recherche français ou étrangers, des laboratoires publics ou privés.

# Conceptual study on nucleation burst evolution in the convective boundary layer – Part III: Physico-chemical characterization

O. Hellmuth

Modelling Department, Institute for Tropospheric Research, Permoser Str. 15, 04318 Leipzig,  
Germany

Received: 1 August 2005 – Accepted: 17 October 2005 – Published: 10 November 2005

Correspondence to: O. Hellmuth (olaf@tropos.de)

© 2005 Author(s). This work is licensed under a Creative Commons License.

## Burst modelling

O. Hellmuth

[Title Page](#)

[Abstract](#)

[Introduction](#)

[Conclusions](#)

[References](#)

[Tables](#)

[Figures](#)

◀

▶

◀

▶

[Back](#)

[Close](#)

[Full Screen / Esc](#)

[Print Version](#)

[Interactive Discussion](#)

EGU

## Abstract

ACPD

5, 11517–11555, 2005

In part I of the present paper a revised columnar high-order model to investigate gas-aerosol interactions in the convective boundary layer (CBL) was proposed. In part II the model capability to predict first-, second-, and third-order moments of meteorological variables in the CBL was demonstrated using available observational data. In the present part, the high-order modelling concept is extended to sulfur and ammonia chemistry as well as to aerosol dynamics. Based on the previous CBL simulation, two conceptual scenarios of the evolution of ultrafine condensation nuclei (UCN) in an anthropogenically influenced CBL are investigated. The scenarios differ in the treatment of new particle formation, whereas homogeneous nucleation according to the classical nucleation theory is considered. The first scenario considers nucleation of a binary system consisting of water vapour and sulfuric acid vapour, the second one on nucleation of a ternary system additionally involving ammonia. Here, the two scenarios are discussed in detail, whereas special attention is paid to the role of turbulence in the formation of the typical UCN burst behaviour, that can often be observed in the Prandtl layer.

## 1. Introduction

Based on the simulation of the evolution of a typical convective boundary layer (CBL) described in part II of this paper, in the present part the physico-chemical conditions of new particle formation (NPF) in the anthropogenically influenced CBL is investigated. Special attention is paid to the interpretation of the time-height cross sections of first- and second-order moments of physico-chemical properties under turbulent conditions. The aim of the present study is to elucidate the role of turbulent diffusion and mixing in the initiation of NPF bursts, that can often be deduced from in situ aerosol measurements performed in the convective Prandtl layer (see the generalized time-evolution pattern in Fig. 1 of part I). Here, the NPF evolution for homogeneous binary

## Burst modelling

O. Hellmuth

[Title Page](#)

[Abstract](#)

[Introduction](#)

[Conclusions](#)

[References](#)

[Tables](#)

[Figures](#)

◀

▶

◀

▶

[Back](#)

[Close](#)

[Full Screen / Esc](#)

[Print Version](#)

[Interactive Discussion](#)

EGU

## 2. Treatment of “spurious oscillations”

In Sect. 3.2.1 of part I the origin of non-physical solutions, so-called spurious oscillations, of the third-order turbulence model and measures to damp them were discussed.

- 5 While the addition of an artificial diffusion term to the right-hand sides of the third-order moment equations was found to efficiently damp such non-physical solutions in the meteorological part of the model, it does not in the physico-chemical part. From a series of numerical experiments it was found, that in the model equations including the full physico-chemical interactions described in the Appendix of part I spurious oscillations
- 10 were already amplified and became dominant after a couple of hours of integration time until an abnormal end of the simulation. Under no circumstances it was possible to find stable solutions of the model system when physico-chemical source/sink terms were considered. The solution was found to be very sensitive against the vertical gradient of the mean physico-chemical variables,  $\partial \bar{\chi}_\alpha / \partial z$ ,  $\alpha=1, \dots, N$ , appearing in the third-order moment equations of Appendix C3 of part I, i.e., in the governing equations for the turbulent transport of scalar fluxes (Appendix C3.2, Eq. (C29)) and the turbulent transport of scalar correlations (Appendix C3.3, Eq. (C32) and Appendix C3.4, Eq. (C35)). To investigate its influence on the evolution of first-, second- and third-order moments a number of runs were performed in which the original mean gradient term
- 15 was “corrected” by an artificial reduction factor, i.e.,  $(1 - C_{12}) \times (\partial \bar{\chi}_\alpha / \partial z)$ ,  $\alpha=1, \dots, N$ , with  $C_{12}$  varying between 0 (original formulation) and 1 (vanishing mean gradient). It was found, that  $C_{12}$  strongly affects the time period during which the solution remains stable. However, the only way to keep the simulation stable over the whole integration time was to set  $C_{12}=1$ . The reason for that behaviour is still not clear. For the time being, the consideration of the reduction factor in front of the mean gradient term
- 20 for the physico-chemical variables is only an ad hoc approach to damp non-physical oscillations. However, in their high-order model [Verver et al. \(1997\)](#), Eq. (8), see refer-

### Burst modelling

O. Hellmuth

[Title Page](#)

[Abstract](#)

[Introduction](#)

[Conclusions](#)

[References](#)

[Tables](#)

[Figures](#)

◀

▶

◀

▶

[Back](#)

[Close](#)

[Full Screen / Esc](#)

[Print Version](#)

[Interactive Discussion](#)

EGU

ences therein) conducted a number of similar simplifications in the governing equation of third-order moments. Among others, the authors neglected all terms of the form  $M_3 \partial M_1 / \partial z$ , where  $M_1$  and  $M_3$  are the averaged first and third moments, respectively: “*It is motivated by the notion that within the bulk of the unstable boundary layer the mean gradient of scalar quantities ( $\partial M_1 / \partial z$ ), as well as terms that contain this gradient, are small*” (Verwer et al., 1997, p. 200–201).

### 3. Parameter dependency of different nucleation mechanisms

Figure 1 shows the parameter dependency of different state-of-the-art nucleation models and parameterizations based on classical nucleation theory, respectively. Kinetic models are not considered. As seen from Fig. 1a, the nucleation rate strongly increases as temperature decreases. At fixed temperature, the various nucleation rate models differ by several orders of magnitude. To note, that the parameterizations of Liu et al. (2001, Eq. (21), “Liu2”) and that of Napari et al. (2002b) are for ternary nucleation at  $\text{NH}_3=0.5$  pptv. As pointed out by Liu et al. (2001), the temperature dependency of the nucleation process is poorly known and theoretical estimates of nucleation rates are notoriously uncertain as well, primarily due to uncertainties in the required thermodynamic data. Therefore, the large variation between different nucleation rates is not surprising but reflects the level of process understanding and parameter knowledge. The humidity dependency is shown in Fig. 1b. For most of the considered models the nucleation rate increases when relative humidity increases as well, except for the ternary nucleation rate of Napari et al. (2002b). For the ternary case Napari et al. (2002a, Figs. 8 and 9) demonstrated, that hydration consumes free sulfuric acid molecules to the extent that nucleation decreases regardless of increasing humidity. This effect was found to be more pronounced at low ammonia concentrations. At low temperatures and high trace gas concentrations the nucleation rate is less dependent on relative humidity (Napari et al., 2002a). In opposite to this, the ammonia-enhanced nucleation rate derived by Liu et al. (2001, Eq. (21), “Liu2”) increases with increasing relative hu-

### Burst modelling

O. Hellmuth

Title Page

Abstract

Introduction

Conclusions

References

Tables

Figures

◀

▶

◀

▶

Back

Close

Full Screen / Esc

Print Version

Interactive Discussion

EGU

midity. At  $RH=0.8$  it is approximately five orders of magnitude larger than that of Napari et al. (2002b). The overall variability between the different models is quite large at fixed humidity as well. The dependency on sulfuric acid vapour is shown in Fig. 1c. The nucleation rate increases as sulfuric acid vapour concentrations increases. As in the foregoing cases, the various nucleation rates differ by several orders of magnitude at fixed acid concentration. Figure 1d shows the dependency of the ternary nucleation rate of Napari et al. (2002b) on the ammonia concentrations for several combinations of temperature, relative humidity and sulfuric acid vapour concentration. In general, the ternary nucleation rate increases with increasing ammonia concentration. Comparing line 1 and 2 in Fig. 1d one can see, that the nucleation rate is very sensitive against the temperature. At fixed ammonia concentration, the nucleation rate increases by approximately five orders of magnitude when temperature decreases by 15 K. A comparison of line 1 and 3 in Fig. 1d shows, that a decrease of the sulfuric acid concentration by one order of magnitude reduces the nucleation rate by approximately five ones. The hydration effect onto the nucleation rate can be seen from the comparison of line 1 and 5 in Fig. 1d. Keeping all other parameters fixed, a reduction of the relative humidity from 0.8 to 0.4 leads to an increase of the nucleation rate by approximately two orders of magnitude.

Summing up it becomes clear, that the nucleation rate model is a highly uncertain and nonlinear parameter function of the present modelling approach. However, while the absolute values of the nucleation rate strongly differ from model to model, the parameter dependencies reflecting the model sensitivity do not. Hence, even if the prediction of UCN number concentration might be very insecure, the spatiotemporal evolution is expected to do not in equal measure.

#### 25 4. Model setup

To investigate NPF events in the anthropogenically influenced CBL, the meteorological simulation described in part II is used as a driving environment for the physico-chemical

O. Hellmuth

[Title Page](#)

[Abstract](#)

[Introduction](#)

[Conclusions](#)

[References](#)

[Tables](#)

[Figures](#)

◀

▶

◀

▶

[Back](#)

[Close](#)

[Full Screen / Esc](#)

[Print Version](#)

[Interactive Discussion](#)

EGU

evolution leading to NPF in the CBL. Figure 2 shows the initial vertical profiles of hydroxyl radical, total ammonia, sulfur dioxide, and sulfuric acid (Fig. 2a), and the number and mass concentration for nucleation, Aitken and accumulation mode aerosols (Figs. 2b, c). The vertical decrease obeys an  $e$ -function according to a characteristic scale height. The background aerosol concentration considered here is quite low. To simplify the chemical reaction system, the evolution of the hydroxyl radical is empirically prescribed. To consider anthropogenic influences, the reservoir of sulfur dioxide and ammonia is permanently supplied with emissions from surface-area sources. With respect to emissions, the federal state Saxony in Germany is considered as a reference region. Covering an area of  $18.413 \text{ km}^2$ , the annual emission strength amounts 10 200 kt/year for sulfur dioxide, and 30 kt/year for total ammonia (gas plus aerosol phase). Therefrom the average emission mass flux can be calculated. For simplicity, the emissions were put into the Prandtl layer at a mean emission rate.

## 5. Evolution of the physico-chemical variables in the CBL

### 15 5.1. First-order moments

#### 5.1.1. Hydroxyl radical (Fig. 3a)

The time-height cross section of the photochemically driven hydroxyl radical concentration is prescribed using an empirical relation (see part I). According to this, the hydroxyl radical exceeds its maximum at noontime, when the solar elevation assumes its maximum as well. During the night, the hydroxyl radical concentration is hold constant at a 20 minimum value.

#### 5.1.2. Sulfur dioxide (Fig. 3b), total and gas-phase ammonia (Figs. 3c, d)

The evolution of sulfur dioxide, total ammonia and gas-phase ammonia corresponds well to the evolution of CBL turbulence. Before sunrise, turbulence is weak and only

## Burst modelling

O. Hellmuth

[Title Page](#)

[Abstract](#)

[Introduction](#)

[Conclusions](#)

[References](#)

[Tables](#)

[Figures](#)

◀

▶

◀

▶

[Back](#)

[Close](#)

[Full Screen / Esc](#)

[Print Version](#)

[Interactive Discussion](#)

EGU

mechanically driven resulting in a very low MLH. Hence, anthropogenic emissions lead to the enhancement of concentrations in the Prandtl layer. In the course of the day, concentrations decrease due to dilution originating from buoyancy-driven turbulence. In the late afternoon turbulence weakens, afterwards a residual layer forms and near-surface concentrations increase again. The evolution of total and gas-phase ammonia proceeds nearly synchronously. The equilibrium gas-phase concentration of ammonia is approximately six orders of magnitude lower than the total ammonia concentration.

### 5.1.3. Sulfuric acid concentration (Figs. 3e, f) and nucleation rate (Figs. 4a, b)

The evolution of sulfuric acid vapour strongly depends on the considered nucleation mechanism. Figure 3e shows the sulfuric acid evolution in the course of the day for binary homogeneous nucleation of sulfuric acid and water vapour. After sunrise, the sulfuric acid concentration starts to rise due to the photochemical oxidation of sulfur dioxide by the hydroxyl radical. When the sulfuric acid concentration exceeds a certain threshold value, noteworthy nucleation can occur, as seen from the time-height cross section of the binary nucleation rate in Fig. 4a. The nucleation occurs in the forenoon within the growing CBL, namely just below the CBL top. The NPF event resembles a “blob”-like pattern in the time-height cross section. According to this, new particle forms in situ in the upper third of the CBL, where temperature is low enough and relative humidity and acidity are high enough to initiate binary nucleation. In the present case, entrainment of ultrafine condensation nuclei (UCN) from the residual layer or free troposphere does not contribute to the aerosol evolution as the initial UCN concentration in the free troposphere is considered to be very low. After new particles were formed and diluted within the developing CBL, the sulfuric acid concentration decreases except for the regions outside the CBL. The newly formed particles within the CBL may serve as a condensation sink for sulfuric acid, leading to a “self-cleansing” of the CBL from condensable gases. Above the CBL this does not happen. When the sulfuric acid concentrations within the CBL drops below a certain threshold binary nucleation immediately breaks up.

## Burst modelling

O. Hellmuth

[Title Page](#)

[Abstract](#)

[Introduction](#)

[Conclusions](#)

[References](#)

[Tables](#)

[Figures](#)

[◀](#)

[▶](#)

[◀](#)

[▶](#)

[Back](#)

[Close](#)

[Full Screen / Esc](#)

[Print Version](#)

[Interactive Discussion](#)

EGU

**Burst modelling**

O. Hellmuth

[Title Page](#)[Abstract](#)[Introduction](#)[Conclusions](#)[References](#)[Tables](#)[Figures](#)[◀](#)[▶](#)[◀](#)[▶](#)[Back](#)[Close](#)[Full Screen / Esc](#)[Print Version](#)[Interactive Discussion](#)

EGU

The evolution of the sulfuric acid concentration for ternary nucleation of water vapour, sulfuric acid and ammonia (Fig. 3f) is qualitatively and quantitatively different from that for the binary case (Fig. 3e). In the ternary case, the maximum of the sulfuric acid concentration is one order of magnitude lower compared to the binary case. This due to the larger condensation sink provided by newly formed particles as well as due to the nucleation loss of sulfuric acid molecules, i.e., the number of molecules consumed in the formation of the critical embryo. Thus, the differences in the sulfuric acid evolution originate from the different nucleation rate evolution. In contrast to the binary nucleation (Fig. 4a), the ternary one assumes its maximum at the top of the model. The maximum itself is three orders of magnitude higher compared to that of the binary nucleation rate. To note, that the parameterization of the ternary nucleation rate cannot be used to obtain the binary water vapour-sulfuric acid or water vapour-ammonia limit. The nucleation rate maximum at the model top mainly reflects the temperature dependency of the nucleation rate parameterization at the ambient sulfuric acid and gas-phase ammonia concentration there. The pattern of the sulfuric acid evolution in the ternary case results from superposition of photochemical activity and CBL turbulence. In the early morning, the sulfuric concentration increases due to photooxidation of sulfur dioxide after sunrise. As the MLH limits the vertical extension of the diffusion domain, sulfur dioxide concentration is enhanced below the MLH due to anthropogenic emissions, hence the sulfuric acid concentration is elevated as well. Above the MLH, the formation of sulfuric acid is limited by the background sulfur dioxide concentration, which is set up by the initial profile of sulfur dioxide. Therefore, the sulfuric acid formation above the MLH is lower to that within the mixing layer. Mainly due to the low temperature, the nucleation rate forms a “virga”-like pattern in the time-height cross section (Fig. 4b), resembling a “sucking tube” at all. The ternary nucleation rate strongly decreases from the top of the model domain toward the Prandtl layer. However, in the course of the day the nucleation starts in the Prandtl layer but not at the top of the model domain. In the Prandtl layer, the temperature is in fact higher compared to that at the top of model domain, hence reducing the nucleation rate. But this damping effect is overcompensated by the enhanced photochemical production of sulfuric acid.

sated by the enhanced near-surface concentration of ammonia and sulfuric acid. Thus, new particles forms at a low rate. Lateron, when sulfuric acid formation increases with the rising sun, the nucleation maximum moves toward the regions of lower temperatures, i.e., toward higher levels. Here, nucleation occurs at much higher rates. In this way, the early start of nucleation in the Prandtl layer and delayed NPF burst above the MLH mainly is an effect of nonlinearity and varying sensitivity of the nucleation rate throughout the input parameter space. When UCN have formed, the further evolution of sulfuric acid is controlled by condensational growth. As the bulk of particles were formed above the MLH, the condensation growth is larger there as well. In the mixing layer, the sulfuric acid concentration is mainly influenced by turbulent dilution. The decrease of sulfuric acid concentration within the CBL in the afternoon corresponds to the cumulative condensation sink there. To note, that the maximum of sulfuric acid concentration in the ternary case is one order of magnitude lower than that in the binary one. This corresponds to the much higher condensation sink in the ternary case, resulting from nucleation at much higher rates.

#### 5.1.4. Number concentration (Figs. 4c–f)

The time-height cross sections of the UCN number concentration for the binary case (Fig. 4c) and for the ternary one (Fig. 4d) corresponds well to those for the considered nucleation rates (Figs. 4a and b, respectively). At first, due to higher efficiency of ternary nucleation the maximum UCN number concentration for the ternary case is three orders of magnitude higher than that for the binary one. Secondly, in the binary case there appears a well-defined burst pattern in the forenoon, characterized by a strong increase between 09:00 and 11:00 LST, exceedance of the maximum around noon, followed by a retarded decrease afterwards. The burst is initiated by the “blob”-like nucleation event (Fig. 4a) just below the top of the growing CBL. Afterwards, newly formed particles were transported downward to the Prandtl layer by CBL turbulence. During the transport, newly formed particles were diluted and well-mixed throughout the CBL column. Once formed, the UCN number concentration immediately begins to

## Burst modelling

O. Hellmuth

[Title Page](#)

[Abstract](#)

[Introduction](#)

[Conclusions](#)

[References](#)

[Tables](#)

[Figures](#)

[◀](#)

[▶](#)

[◀](#)

[▶](#)

[Back](#)

[Close](#)

[Full Screen / Esc](#)

[Print Version](#)

[Interactive Discussion](#)

EGU

---

**Burst modelling**

O. Hellmuth

[Title Page](#)[Abstract](#)[Introduction](#)[Conclusions](#)[References](#)[Tables](#)[Figures](#)[◀](#)[▶](#)[◀](#)[▶](#)[Back](#)[Close](#)[Full Screen / Esc](#)[Print Version](#)[Interactive Discussion](#)

EGU

decrease due to intramode and intermode coagulation and deposition. In the ternary case, the time-height evolution of UCN number concentration (Fig. 4d) corresponds quite good to the associated nucleation pattern as well. In the Prandtl layer, the UCN number concentration starts to rise immediately after sunrise due to in situ ternary nucleation. Following the “sucking tube”-like evolution pattern of the ternary nucleation rate (Fig. 4b), the UCN number concentration assumes a temporally broadened maximum at the top of the model domain in the forenoon. From there, the UCN number concentration decreases toward the CBL. Once captured by entrainment processes, newly formed particles enters the CBL, where they were diluted and well-mixed. Downward diffusion of entrained UCN enhances the UCN number concentration in the Prandtl layer. According to this scenario, NPF starts in situ in the Prandtl layer in the early morning, afterwards enhanced by downward transport of entrained UCN. Outside the CBL, the UCN concentration pattern is not blurred, as turbulent diffusion is small there. As for the binary case, the UCN concentration decreases within the CBL in the course of the day by intramode and intermode coagulation and deposition as well. The time-height evolution of the number concentration of the Aitken mode (Fig. 4e) and accumulation mode particles (Fig. 4f) for binary nucleation is nearly identical to that for ternary one (not shown). This is plausible as coagulation with UCN particles does not change the number concentration of pre-existing Aitken and accumulation mode particles, since the particle number in the corresponding larger modes is conserved when larger particles collide with smaller ones. The time-height cross section of number concentrations corresponds well to the CBL evolution in general. At the initial state, the number concentration of pre-existing Aitken and accumulation mode particles decreases with height. In the Prandtl layer, the Aitken number concentration already decreases due to deposition at nighttime. Because of the size-dependency of the deposition velocity, deposition of accumulation mode particles is much smaller. When turbulence set in, the pre-existing Aitken and accumulation mode particles are diluted throughout the mixing layer, leading to well-mixed vertical distribution. The temporal decrease of number concentration in both modes is due to intramode and intermode

---

**Burst modelling**O. Hellmuth

---

[Title Page](#)[Abstract](#)[Introduction](#)[Conclusions](#)[References](#)[Tables](#)[Figures](#)[◀](#)[▶](#)[◀](#)[▶](#)[Back](#)[Close](#)[Full Screen / Esc](#)[Print Version](#)[Interactive Discussion](#)

EGU

coagulation. There are only very small differences in the coagulation loss, resulting from the impact of particle radius onto the coagulation coefficient. The particle radius is diagnostically determined from number and mass concentration. For Aitken mode particles, the coagulation loss is slightly enhanced for the ternary case compared to the binary one. However, for accumulation mode particles there are no observable differences between the evolution patterns of the binary and ternary case, respectively.

### 5.1.5. Mass concentration (Figs. 5a–f)

The mass concentrations of UCN, Aitken and accumulation mode particles significantly differ for binary and ternary nucleation, respectively. The time-height cross section 10 of the UCN mass concentration in the binary case (Fig. 5a) corresponds well to the pattern of the sulfuric acid concentration (Fig. 3e) and UCN number concentration (Fig. 4c). A significant gain of particle mass by sulfuric acid condensation can be firstly observed after UCN number concentration has exceed its maximum. Hence, the temporal progression of cleansing the CBL from condensable sulfuric acid vapour for 15 binary nucleation might be thought as follows:

1. Increase of the hydroxyl radical concentration after sunrise;
2. Initiation of sulfuric acid production with subsequent exceedance of a critical sulfuric acid vapour threshold;
3. Onset of an elevated “blob”-like nucleation burst just below the top of the developing CBL, followed by turbulence-induced downward transport of UCN leading to a well-mixed vertical UCN profile;
4. Subsequent increase of UCN number concentration throughout the CBL until a certain level for initiation of condensation growth has reached;
5. Onset of significant UCN mass accumulation due to sulfuric acid condensation throughout the entire CBL;

- 5  
6. Decrease of UCN number concentration due to intramode and intermode coagulation, decrease of sulfuric acid vapour concentration due to deposition loss of vapour molecules onto newly formed particles as well as onto pre-existing Aitken and accumulation mode particles leading to condensation vapour cleansing of the CBL.

10

15

20

25

For the ternary case, the evolution pattern of UCN mass concentration (Fig. 5b) is qualitatively similar to that for the binary case (Fig. 5a), except for the start-up phase of condensation growth. The difference between the daytime maxima of UCN mass concentration is small. However, due to in situ ternary nucleation in the Prandtl layer in the early morning a much higher UCN number concentration compared to the binary case is available to serve as a condensation sink already at that time. Hence, mass accumulation by sulfuric acid condensation growth can start earlier too. To note, that owing to the formation of new particles above the CBL, mass accumulation occurs there as well. Nonetheless, the mass accumulation within the CBL exceeds that in the free troposphere since much more condensable vapour is available within the CBL originating from low-level emission of the precursor gas sulfur dioxide and subsequent photooxidation to produce sulfuric acid vapour. CBL turbulence ensures, that condensation sinks and condensable vapour are well-mixed throughout the CBL, hence vertically homogenizing the UCN mass distribution within the mixing layer. The differences in UCN number concentration for the binary and ternary case, respectively, can be directly persecuted in the mass concentrations of pre-existing Aitken (Figs. 5c, d) and accumulation mode particles (Figs. 5e, f) as well. These two modes serve as a coagulation sink for the respective smaller modes, and as a deposition sink for condensable vapours as well. Hence, differences in UCN number concentration should be carried forward across the mode cascade, i.e., from the smallest mass concentration mode toward the largest one according to the law of error propagation. This can be seen in the mass concentrations of the Aitken and accumulation mode. In the ternary case, the maximum mass concentration of both modes is somewhat lower compared to the corresponding binary cases. This can be explained by the lower supply with

## Burst modelling

O. Hellmuth

[Title Page](#)

[Abstract](#)

[Introduction](#)

[Conclusions](#)

[References](#)

[Tables](#)

[Figures](#)

[◀](#)

[▶](#)

[◀](#)

[▶](#)

[Back](#)

[Close](#)

[Full Screen / Esc](#)

[Print Version](#)

[Interactive Discussion](#)

EGU

condensable vapour in the ternary case (see sulfuric acid concentration in Figs. 3e, f) originating from larger nucleation loss of sulfuric acid molecules to form a critical embryo. In the ternary case, more sulfuric acid molecules are consumed in the formation of new embryos rather than condensed onto the pre-existing aerosol surface. To note, 5 that the number concentration of pre-existing aerosols was chosen to be very low at the initial state. The net accumulation of condensable vapours in these modes competes with that in the nucleation mode, and uncertainties in the sulfuric acid vapour evolution may become crucial in the mass balance of the pre-existing aerosols as well. Anyway, the main difference between the time-height evolution of the Aitken and accumulation 10 mode concentration of the binary and the ternary case, respectively, consists in the earlier begin of the mass accumulation. The explanation of the quantitative differences deserve further investigations.

## 5.2. Second-order moments

### 5.2.1. Remarks

15 From the large number of predictive second-order moments only those are depicted, which can be interpreted with respect to NPF events in the CBL. In opposite to the meteorological variables, empirical findings on second-order moments of physico-chemical variables are still very scarce. However, the simulation results will be compared with previous findings as far as possible.

### 20 5.2.2. Turbulent vertical flux

Although not possible to be verified by observations, the turbulent vertical flux of total ammonia (Fig. 6a) and sulfur dioxide (Fig. 6b) corresponds well to the flux pattern of non-reactive scalars expectable in the CBL. In both cases, the flux is always positive within the CBL in the course of the day except for the lowest half-level where it becomes 25 negative owing to dry deposition. The turbulent transport is upward directed because

## Burst modelling

O. Hellmuth

[Title Page](#)

[Abstract](#)

[Introduction](#)

[Conclusions](#)

[References](#)

[Tables](#)

[Figures](#)

[◀](#)

[▶](#)

[◀](#)

[▶](#)

[Back](#)

[Close](#)

[Full Screen / Esc](#)

[Print Version](#)

[Interactive Discussion](#)

EGU

**Burst modelling**

O. Hellmuth

[Title Page](#)[Abstract](#)[Introduction](#)[Conclusions](#)[References](#)[Tables](#)[Figures](#)[◀](#)[▶](#)[◀](#)[▶](#)[Back](#)[Close](#)[Full Screen / Esc](#)[Print Version](#)[Interactive Discussion](#)

EGU

the chemical species were released into the Prandtl layer, hence the concentrations of the species decrease with height. The vertical flux pattern of the pseudo-reactive sulfuric acid vapour is much more complicated and reveals strong differences between the binary (Fig. 6c) and ternary case (Fig. 6d). In the binary case, the initial vertical flux is zero at all height. When CBL turbulence set in, the vertical flux becomes greater zero, indicating a weak upward transport of sulfuric acid. Later on, when CBL turbulence intensifies, a shallow layer of downward directed turbulent flux forms in the lowest model layers while above the positive flux strengthens. Between 09:00 and 12:00 LST, the photochemically produced sulfuric acid vapour concentration exceeds its maximum and shows a well-mixed vertical distribution throughout the CBL. The occurrence of the positive flux maximum spatiotemporally coincides with the “blob”-like binary nucleation event (Figs. 4a, c). The level of “zero flux” represents the location of an “apparent pseudo-reaction source” (net source), from which the considered species is upward and downward diluted by turbulence. The vertical flux of sulfuric acid vapour weakens, when condensation and “self-cleansing” of the CBL set in. In the late afternoon, a secondary positive flux maximum forms. To note, that the flux evolution of sulfuric acid vapour is not only affected by turbulent diffusion, but essentially by higher-order moments resulting from physico-chemical interaction terms in the non-filtered governing equation as well. For the ternary case, the evolution pattern of sulfuric acid vapour (Fig. 6d) quantitatively differs from that for the binary one, but in the general the basic features qualitatively agree, as shown afterwards. When ternary nucleation starts in the early morning in the Prandtl layer, a similar vertical downward/upward flux pattern as in the binary case appears there, but at a smaller time and spatial scale. This supports the assumption, that the vertical flux layering is strongly related to the nucleation loss of sulfuric acid molecules. In opposite to the binary case, the vertical flux evolves later on toward a primary positive maximum throughout the CBL except for the Prandtl layer. While in the binary case the vertical flux suddenly decreases when condensation loss of sulfuric acid vapour onto particles becomes important, in the ternary case they do not. This is due to the lower impact of condensation loss onto newly formed

particles, which were mainly formed outside the CBL in the ternary case.

Hence, the evolution pattern of the sulfuric acid vapour flux can be generalized as follows: (a) Vertical two-layer flux pattern (downward/upward flux) in the prenucleation phase and during the NPF event; (b) Subsequent upward directed vapour flux in the postnucleation phase of condensation growth.  
5

The absolute values of the vertical flux as well as the extension and spatiotemporal distribution of the flux minima and maxima in the evolution pattern are strongly affected by physico-chemical interactions, i.e., nucleation and condensation loss of sulfuric acid vapour molecules, which are usually neglected in diagnostic downgradient flux parameterizations.  
10 A comparison with the plain structure of the time-height cross section of the non-reactive species ammonia (Fig. 6a) and sulfur dioxide (Fig. 6b) shows, that additional correlation terms resulting from the gas-aerosol interactions, e.g., as appearing in the governing equation of the sulfuric acid flux, may have a significant impact on the flux evolution, especially, when highly nonlinear processes such as nucleation and condensation are involved.  
15 For the time being, a direct verification of the flux of sulfuric acid vapour must fail due to lack of corresponding observational data. To note, that vertical profiling of sulfuric acid vapour concentration in the CBL is generally hard to realize. Apart from that it is much more difficult to measure highly-resolved spatio-temporal data series of precursor gases to derive flux profiles. However, perhaps the present modelling approach provides some motivation to determine high-order moments involving  
20 physico-chemical species from in situ measurements or remote sensing as well.

The time-height evolution of the turbulent vertical flux of the UCN number concentration for the binary case (Fig. 6e) and for the ternary one (Fig. 6f) are closely correlated to the corresponding evolution pattern of the nucleation rate (Figs. 4a, b) and the UCN number concentration (Figs. 4c, d). In the binary case, the level of “zero UCN flux” coincides well in time and space with the “blob”-like source of newly formed particles (Fig. 4a). From there, the bulk of UCN is transported downward ( $w'N'_1 < 0$ ), a certain part is transported upward ( $w'N'_1 > 0$ ) and diluted throughout the entrainment layer. As shown below, this downward directed flux leads to a sudden enhancement of UCN  
25

## Burst modelling

O. Hellmuth

[Title Page](#)

[Abstract](#)

[Introduction](#)

[Conclusions](#)

[References](#)

[Tables](#)

[Figures](#)

[◀](#)

[▶](#)

[◀](#)

[▶](#)

[Back](#)

[Close](#)

[Full Screen / Esc](#)

[Print Version](#)

[Interactive Discussion](#)

EGU

number concentration in the Prandtl layer, representing the “NPF burst” in a closer sense. According to the binary scenario conceived here, these bursts do not originate from in situ nucleation within the Prandtl layer but can be ascribed to downward transport of UCN recently formed in the upper third of the forenoon CBL. In the ternary case, the flux pattern (Fig. 6f) reflects the progression of the NPF event (Figs. 4b, d) very good as well. Here, the above-described downward/upward flux layering occurs in the early morning, when the CBL just starts to rise. Hence, the downward flux is restricted to occur in the lowest model layers, i.e., at lower time and spatial scales. Once in situ formed there, UCN are immediately transported downward to the surface and upward into the entrainment layer by the developing CBL turbulence. This flux pattern corresponds well to that in the binary case, except that it occurs at smaller time and spatial scales. Shortly after initial NPF at low levels, the lower end of the “sucking tube”-like NPF pattern above the CBL merges with the preceding in situ nucleation. The subsequent downward transport of UCN, continuing during the forenoon, reflects the dilution of entrained UCN from above. The absolute minimum of the UCN flux appears, when the UCN “sucking tube” enters the MLH and it is being captured by CBL turbulence. Afterwards, the downward flux decreases as the number of entrained UCN decreases as well. Supposed that the time-height evolution of the UCN formation rate is appropriately represented by the parameterization of the ternary nucleation rate, then the vertical UCN flux pattern in Fig. 6f consistently behaves with respect to CBL turbulence and to the evolution of the UCN number concentration as well. Apart from qualitative differences, the absolute value of the UCN flux for the ternary case is by several orders of magnitude larger than that for the binary case. While CBL turbulence is identical in both cases, the turbulent vertical flux of UCN number concentration is higher for the ternary case.

### 5.2.3. Cross-correlations

$\theta' \text{NH}_{3,\text{tot}}'$  (Fig. 7a):

---

## Burst modelling

O. Hellmuth

---

[Title Page](#)

[Abstract](#)

[Introduction](#)

[Conclusions](#)

[References](#)

[Tables](#)

[Figures](#)

◀

▶

◀

▶

[Back](#)

[Close](#)

[Full Screen / Esc](#)

[Print Version](#)

[Interactive Discussion](#)

EGU

In the entrainment layer the potential temperature and the total ammonia concentration are anticorrelated ( $\theta'NH_{3,tot}' < 0$ ), indicating entrainment of potentially warmer but ammonia-depleted free-tropospheric air into the CBL and/or detrainment of potentially colder but ammonia-enriched CBL air into the free troposphere.

5

$q'NH_{3,tot}'$  (Fig. 7b):

In opposite to this, the water vapour mixing ratio and the total ammonia concentration are positively correlated in the entrainment layer ( $q'NH_{3,tot}' > 0$ ), resulting from entrainment of drier and ammonia-depleted free-tropospheric air into the CBL and/or detrainment of moistier and ammonia-enriched CBL air into the free troposphere.

10

$\theta'H_2SO_4'$  (Figs. 7c, d):

15

The correlation of potential temperature and sulfuric acid vapour for the binary and ternary case are strongly different. In the binary case, the correlation in the entrainment layer changes its sign in the course of the day (Fig. 7c). In the forenoon, sulfuric acid vapour is photochemically produced in the CBL, exceeding its maximum there (Fig. 3e). Hence, during the oxidation time turbulence causes entrainment of potentially warmer but sulfuric acid vapour-depleted free-tropospheric air and/or detrainment of potentially colder but sulfuric acid vapour-enriched CBL air into the free troposphere ( $\theta'H_2SO_4' < 0$ ). Lateron, after nucleation had occurred, condensation sink becomes more and more important leading to a decrease of sulfuric acid vapour within the CBL. Above the CBL, UCN concentration is quite low, hence not serving as condensation sink for sulfuric acid vapour. As a result, the sulfuric acid vapour concentrations in the free troposphere is slightly higher compared to that in the CBL. Under such circumstances, turbulence consequently leads to the entrainment of potentially warmer and sulfuric acid vapour-enriched free-tropospheric air into the CBL and/or detrainment of potentially colder and sulfuric acid vapour-depleted CBL

20

25

## Burst modelling

O. Hellmuth

[Title Page](#)

[Abstract](#)

[Introduction](#)

[Conclusions](#)

[References](#)

[Tables](#)

[Figures](#)

[◀](#)

[▶](#)

[◀](#)

[▶](#)

[Back](#)

[Close](#)

[Full Screen / Esc](#)

[Print Version](#)

[Interactive Discussion](#)

EGU

air into the free troposphere ( $\theta' \text{H}_2\text{SO}_4' < 0$ ). Thus, the time when the cross correlation changes its sign indicates the moment, when the sulfuric acid vapour condensation sink becomes important. In the ternary case, the corresponding correlation in the entrainment layer remains negatively during the day, showing a well-distinguished negative maximum (absolute minimum) in the early morning, which is separated from a second, more extended one lasting from forenoon until afternoon (Fig. 7d). The zone of anticorrelation is related to the entrainment of potentially warmer but sulfuric acid vapour-depleted free-tropospheric air into the CBL and/or to detrainment of potentially colder but sulfuric acid vapour-enriched CBL air into the free troposphere.

As ternary nucleation exceeds its maximum outside the CBL, the sulfuric acid vapour condensation sink assumes its maximum there as well. Hence, the sulfuric acid vapour concentration in the CBL remains always higher than in the free troposphere (Fig. 3f). The transition between the two pronounced anticorrelation periods, appearing at 07:00 LST, marks the temporal crossover from in situ NPF in the morning Prandtl layer to the forenoon entrainment of UCN recently formed above the CBL and downward transported from there. At the crossover time, sulfuric acid vapour condensation sink becomes important, leading to a decrease of sulfuric acid vapour concentration. Shortly after the “sucking tube” of the UCN pattern (Fig. 4d) has entered the Prandtl layer from above the sulfuric acid vapour concentration increases again.

$q' \text{H}_2\text{SO}_4'$  (Figs. 7e, f):

The correlation of water vapour mixing ratio and sulfuric acid vapour corresponds very well to the  $\theta' \text{H}_2\text{SO}_4'$  pattern. Considering that potential temperature and water vapour mixing ratio are anticorrelated throughout the entrainment layer, the “quasi-reversed” behaviour of the corresponding pattern pairs Figs. 7c, e and Figs. 7d, f is self-evident.

$\theta' N'_1$  (Figs. 8a, b):

## Burst modelling

O. Hellmuth

[Title Page](#)

[Abstract](#)

[Introduction](#)

[Conclusions](#)

[References](#)

[Tables](#)

[Figures](#)

[◀](#)

[▶](#)

[◀](#)

[▶](#)

[Back](#)

[Close](#)

[Full Screen / Esc](#)

[Print Version](#)

[Interactive Discussion](#)

EGU

The evolution pattern of cross-correlation of potential temperature and UCN number concentration are quite different for the binary and ternary case. For binary nucleation, the potential temperature and UCN number concentration are anticorrelated in the entrainment layer (Fig. 8a), i.e., negative potential temperature fluctuations are positively correlated with positive fluctuations of UCN number concentration. In other words, low potential temperature favours the occurrence of UCN. The location and time of occurrence of the absolute minimum of  $\overline{\theta'N'_1}$  coincides more or less with the NPF event and reflects to some degree the dependency of the nucleation rate on temperature. More importantly, the occurrence of positive correlations within the entrainment layer in the course of the day indicates detrainment of potentially colder but UCN-enriched CBL air into the free troposphere and/or entrainment of potentially warmer but UCN-depleted free-tropospheric air into the CBL. For the ternary case, the absolute minimum of  $\overline{\theta'N'}$  in the early morning corresponds well to the low-level in situ formation of NPF (Fig. 8b). The subsequent positive correlation of potential temperature and UCN number concentration reflects the coinciding entrainment of potential warmer and UCN-enriched residual-layer air into the CBL, the latter resulting from ternary nucleation above.

$\overline{q'N'_1}$  (Figs. 8c, d):

In the same way the correlation of water vapour mixing ratio and UCN number concentration can be interpreted. For the binary case, the water vapour mixing ratio is positively correlated with the UCN number concentration in the entrainment layer, i.e., positive humidity fluctuations are associated with positive fluctuations in UCN number concentration (Fig. 8c). This behaviour is inverse to the  $\overline{\theta'N'_1}$  correlation pattern and can be partially ascribed to the enhancement of nucleation due to increased humidity. However, the concurrence of the positive correlation regime with the entrainment layer indicates entrainment of drier and UCN-depleted free-tropospheric air into the CBL

## Burst modelling

O. Hellmuth

[Title Page](#)

[Abstract](#)

[Introduction](#)

[Conclusions](#)

[References](#)

[Tables](#)

[Figures](#)

[◀](#)

[▶](#)

[◀](#)

[▶](#)

[Back](#)

[Close](#)

[Full Screen / Esc](#)

[Print Version](#)

[Interactive Discussion](#)

EGU

and/or detrainment of moistier and UCN-enriched CBL air into the free troposphere. The inverse correlation pattern in the  $\theta'N'_1$  and  $q'N'_1$  time-height cross section observed for the binary case appears for the ternary one as well (Fig. 8d). In the early morning, the water vapour mixing ratio is positively correlated with the UCN number concentration indicating favoured ternary nucleation due to enhanced humidity at that time. Later on, entrainment of drier but UCN-enriched free-tropospheric air becomes dominant, leading to  $q'N'_1 < 0$  in the entrainment layer. Hence, the  $\theta'N'_1$  and  $q'N'_1$  evolution are in each case consistent with the overall evolution of CBL turbulence and the supposed nucleation mechanism.

10

$NH_{3,tot}'N'_1$  (Figs. 9a, b):

The cross-correlation of total ammonia and UCN number concentration strongly differs for the binary and ternary case. In the binary case, the total ammonia concentration is positively correlated with UCN number concentration in the entrainment layer after nucleation has occurred. This positive correlation in the late forenoon indicates detrainment of total ammonia and UCN-enriched CBL air into the free troposphere and/or entrainment of free-tropospheric air depleted from total ammonia and UCN into the CBL ( $NH_{3,tot}'N'_1 > 0$ ). The positive correlation sets firstly on when new particles were formed. The same happens for the ternary case too, but here the strongest positive correlation already occurs in the early morning, when the MLH is very low and the concentration of total ammonia from surface emission sources is relatively high.

## Burst modelling

O. Hellmuth

[Title Page](#)

[Abstract](#)

[Introduction](#)

[Conclusions](#)

[References](#)

[Tables](#)

[Figures](#)

◀

▶

◀

▶

[Back](#)

[Close](#)

[Full Screen / Esc](#)

[Print Version](#)

[Interactive Discussion](#)

EGU

## $H_2SO_4'N'_1$ (Figs. 9c, d):

As for the antecedent correlation pair, the cross-correlations of sulfuric acid vapour and UCN number concentration for the binary and ternary case strongly differ. In the 5 binary case,  $H_2SO_4'N'_1 > 0$  with a pronounced maximum in the forenoon just below the MLH (Fig. 9c), where binary NPF occurs (Figs. 4a, c). To enable nucleation to occur, the sulfuric acid vapour concentration must exceed a certain threshold (Fig. 3e). The positive correlation between sulfuric acid vapour and UCN number concentration reflects the entrainment of UCN and sulfuric acid vapour-poor free-tropospheric air into the 10 CBL and/or detrainment of UCN and sulfuric acid vapour-enriched CBL air into the free troposphere. In the ternary case, the  $H_2SO_4'N'_1$  correlation corresponds well to the pattern shown in Fig. 9b. The UCN particles newly formed in situ in the Prandtl layer in the early morning are positively correlated with the sulfuric acid vapour, which starts to be formed from photolytical oxidation of sulfur dioxide and hydroxyl radical. At that 15 time, the sulfur dioxide concentration originating from surface emissions is enhanced due to the low MLH. Even if the hydroxyl radical concentration is still low, sulfuric acid vapour starts to form and fill the CBL reservoir until NPF sets on. Hence,  $H_2SO_4'N'_1 > 0$  occurring in the early morning indicates turbulence-induced entrainment of sulfuric acid vapour and UCN-poor residual-layer air into the growing CBL and/or detrainment of 20 sulfuric acid vapour and UCN-enriched CBL air into the residual layer.

### 5.3. Physico-chemical variables in the Prandtl layer

The time series of physico-chemical variables in the Prandtl layer are shown in Figs. 10 to 12. The evolution of gas-phase species near the surface is depicted in Fig. 10a. The devolution of sulfur dioxide and total ammonia is controlled by the interplay between emission and dilution. Owing to the larger emission, the sulfur dioxide concentration is always larger than that of total ammonia. In the morning hours, the corresponding concentrations are enhanced due to emission into the Prandtl layer with weak turbu-

## Burst modelling

O. Hellmuth

[Title Page](#)

[Abstract](#)

[Introduction](#)

[Conclusions](#)

[References](#)

[Tables](#)

[Figures](#)

[◀](#)

[▶](#)

[◀](#)

[▶](#)

[Back](#)

[Close](#)

[Full Screen / Esc](#)

[Print Version](#)

[Interactive Discussion](#)

EGU

---

**Burst modelling**

O. Hellmuth

[Title Page](#)[Abstract](#)[Introduction](#)[Conclusions](#)[References](#)[Tables](#)[Figures](#)[◀](#)[▶](#)[◀](#)[▶](#)[Back](#)[Close](#)[Full Screen / Esc](#)[Print Version](#)[Interactive Discussion](#)

EGU

lence. In the course of the day, the concentrations decrease owing to turbulence-induced dilution. In the evening, when the mixed layer collapses, concentrations increase again. The gas-phase concentration of ammonia, obtained from the equilibrium aerosol model, follows strongly the total ammonia devolution. The gas-phase concentration of ammonia is by several orders of magnitude lower than the total ammonia concentration. The hydroxyl radical concentration from the semi-empirical model follows the solar elevation, i.e., reaching its maximum around noon. The sulfuric acid vapour concentration is closely correlated to the concentration of the hydroxyl radical. For the ternary case, sulfuric acid vapour concentration is lower due to higher condensation sink, represented by higher UCN number concentration. In Fig. 10b, relative humidity and relative acidity are shown. The relative humidity peaks in the morning and evening hours, mainly controlled by the temperature devolution. In the course of the day, the relative humidity decreases due to turbulent mixing and solar-induced warming. The relative acidity devolution corresponds well to the sulfuric acid vapour concentration in Fig. 10a. Due to the temperature dependency, it strongly decreases during the course of the day. As a consequence of higher condensation sink, the relative acidity is much lower in the ternary case. Figure 10c shows the time series of the nucleation rate in the Prandtl layer. The ternary nucleation rate is a few orders of magnitude larger than the binary one. The cut-off at  $J_{\text{nuc}}=10^{-5} \text{ cm}^{-3}\text{s}^{-1}$  denotes the limits of the validity of the parameterization (Napari et al., 2002b). While the ternary nucleation rate gives a signal of in situ NPF in the morning hours, the binary one does not ( $J_{\text{nuc}}<10^0 \text{ cm}^{-3}\text{s}^{-1}$ ). Figure 11 shows the time series of the number and mass concentration of UCN, Aitken and accumulation mode particles. In connection with the related time-height cross sections, the typical devolution pattern of the UCN number concentration in Fig. 11a allows to deduce the origin of UCN observable in the Prandtl layer. The ternary-case pattern reveals a pronounced burst in the early morning, when the ternary nucleation rate (Fig. 10c) peaks as well. Afterwards, the UCN number concentration decreases due to intra- and intermode coagulation. The lack of a second peak when turbulence becomes important points to in situ, i.e., local NPF controlled by enhanced ammonia

---

**Burst modelling**

O. Hellmuth

[Title Page](#)[Abstract](#)[Introduction](#)[Conclusions](#)[References](#)[Tables](#)[Figures](#)[◀](#)[▶](#)[◀](#)[▶](#)[Back](#)[Close](#)[Full Screen / Esc](#)[Print Version](#)[Interactive Discussion](#)

EGU

concentration in the morning Prandtl layer. In opposite to this, the binary-case pattern reveals a pronounced, but much lower burst at a time, when the binary nucleation rate in the Prandtl layer is subcritical but CBL turbulence becomes important. This pattern points to ex-situ, i.e., non-local NPF in upper parts of the CBL followed by turbulent downward transport of UCN. The antecedent secondary peak in the morning hours is formed in situ due to temporally enhanced relative humidity and relative acidity and low temperature. To note, the foregoing peak is by several orders of magnitude lower than the subsequent primary peak. The differences in the devolution of the UCN mass concentration seen in Fig. 11b results from the different burst pattern as well as from subsequent condensation growth. Thus, in the ternary case UCN are formed at a much earlier time, hence starting earlier to consume sulfuric acid vapour for particle growth by condensation. In opposite to this, in the binary case the bulk of UCN are formed at a later time at a much lower rate. Therefore, condensation growth proceeds at a lower rate. The devolution of number concentration of Aitken and accumulation mode aerosols in Figs. 11c, e can be explained by the interplay of deposition, entrainment and intra- and intermode coagulation. The initial nighttime value of the pre-existing Aitken mode number concentration is very low (Fig. 11c). It strongly decreases due to the dominant effect of dry deposition. When the CBL starts to grow, the Aitken mode aerosols are entrained from above into the Prandtl layer, leading to a jump in the time series of number concentration in the early morning. The further devolution is controlled by intra- and intermode coagulation loss, deposition and turbulent mixing. In the binary case, the decrease of Aitken mode number concentration is weaker than in the ternary case due to a somewhat lower coagulation rate. The coagulation rate depends on the particle radius that is diagnostically determined from mass and number concentration. The devolution of accumulation mode number concentration in Fig. 11e is quite similar and controlled by the same processes. The differences in the evolution of mass concentration of the Aitken and accumulation mode between the binary and ternary case according to Figs. 11d, f originate from the competition of the condensation growth in these two modes with the that in the UCN mode. In the ternary case,

the early start of NPF and subsequent condensation growth of UCN (Fig. 11b) reduces the sulfuric acid vapour amount available for further growth and mass accumulation of pre-existing aerosols. Considering the different scales in Figs. 11b, d, f one can see that the mass concentration of accumulation mode aerosols in Fig. 11f undergoes a  
5 jump in its time series in the early morning as well.

Figure 12 shows the turbulent vertical flux of UCN number concentration in the Prandtl layer for the binary and ternary case. In each case there appears a pronounced peak of the downward directed UCN flux coinciding with the corresponding primary NPF burst. In the binary case, the downward UCN flux maximum at forenoon  
10 coincides with the “blob”-like NPF evolution pattern appearing in Figs. 4a, c and corresponds with the time-height cross section of UCN flux in Fig. 6e. Analogous in the ternary case, there is a coincidence of the maximum of downward UCN flux with the “sucking tube”-like NPF evolution pattern depicted in Figs. 4b, d, which corresponds with the time-height cross section of the UCN flux in Fig. 6f.

## 15 6. Summary and conclusion

The model approach presented here is suitable to simulate NPF bursts in the CBL. The intercomparison of a typical binary and ternary NPF scenario in the anthropogenically influenced CBL using state-of-the-art nucleation models shows large differences in the evolution of the UCN number concentration in the Prandtl layer as well as in the time-  
20 height cross sections of first-order moments and double correlation terms. Although in both cases the occurrence of NPF bursts could be simulated, the burst characteristics and genesis of the bursts are completely different. It was demonstrated, that observations from the Prandtl layer alone are not conclusive to elucidate the origin of newly formed particles. This is also true with respect to the interpretation of box modelling studies.  
25 The binary and ternary NPF bursts observed in the Prandtl layer differ with respect to burst amplitude and phase. In the considered binary scenario the burst evolution is a direct result of the interaction of photochemically produced sulfuric acid vapour

### Burst modelling

O. Hellmuth

[Title Page](#)

[Abstract](#)

[Introduction](#)

[Conclusions](#)

[References](#)

[Tables](#)

[Figures](#)

[◀](#)

[▶](#)

[◀](#)

[▶](#)

[Back](#)

[Close](#)

[Full Screen / Esc](#)

[Print Version](#)

[Interactive Discussion](#)

EGU

**Burst modelling**

O. Hellmuth

[Title Page](#)[Abstract](#)[Introduction](#)[Conclusions](#)[References](#)[Tables](#)[Figures](#)[◀](#)[▶](#)[◀](#)[▶](#)[Back](#)[Close](#)[Full Screen / Esc](#)[Print Version](#)[Interactive Discussion](#)

EGU

and CBL turbulence. New particles are formed in the forenoon in the upper part of the growing CBL, followed by turbulence-induced top-down transport. Hence, with respect to the burst observation site in the Prandtl layer, new particles are formed ex situ. In opposite to this, the ternary case reveals a much more complex pattern. Here, NPF is  
5 much less controlled by sulfuric acid vapour. NPF is initiated in the early morning hours in the Prandtl layer, when temperature is low and relative humidity, sulfur dioxide and ammonia concentration are high, hence being in situ formed. The damping effect of the low sulfuric acid concentration onto the nucleation rate at that time is overcompensated mainly by the forcing effect of the enhanced ammonia concentration. Shortly after that,  
10 ex situ NPF in the free troposphere set in, followed by entrainment and top-down diffusion of newly formed particles into the Prandtl layer. Altogether, these processes mainly contribute to the formation of a strong burst in the morning hours. The ternary case simulation shows, that ammonia not only serves as a constant offset or tuning parameter in nucleation models but undergoes a diurnal evolution strongly controlled  
15 by CBL turbulence. Hence, its impact on the burst evolution is nonlinear. While the time-height cross section of the binary nucleation rate resembles a “blob”-like evolution pattern, the ternary one resembles a “sucking tube”-like pattern. The time-height cross sections of the flux pattern and double correlations could be plausibly interpreted in terms of CBL turbulence and entrainment/detrainment processes both in the binary  
20 as well as in the ternary case. The simulations provide a number of predictive high-order moment, that can not yet be directly verified by observational data. However, these fields behave reasonably and give insight in the genesis of NPF in the boundary layer. Although the simulated scenarios claim to consider typical conditions leading to NPF bursts, they are restricted to classical homogenous nucleation involving only up to  
25 three species (water vapour, sulfuric acid vapour, ammonia) and consider only a special emission scenario and concentration background. Nevertheless, the interaction between CBL turbulence, sulfur and ammonia chemistry and aerosol dynamics could be simulated using a self-consistent modelling approach. Apart from a comprehensive model verification/validation further scenario simulations are necessary to systemat-

ically verify or falsify, respectively, the number of state-of-the-art hypothesis on NPF currently under discussion. In part IV of the paper an attempt is made to reevaluate previous observations of NPF in the CBL with respect to the two scenarios investigated here.

## 5 References

- Jaecker-Voirol, A. and Mirabel, A. P.: Nucleation rate in a binary mixture of sulfuric acid and water vapor, *J. Phys. Chem.*, 92, 3518–3521, 1988. [11544](#)
- Jaecker-Voirol, A. and Mirabel, A. P.: Heteromolecular nucleation in the sulfuric acid-water system, *Atmos. Environ.*, 23, 2053–2057, 1989. [11544](#)
- Jaeger-Voirol, A., Mirabel, A. P., and Reiss, H.: Hydrates in supersaturated binary sulfuric acid-water vapor: A re-examination, *J. Chem. Phys.*, 87, 4849–4852, 1987. [11544](#)
- Kulmala, M. and Laaksonen, A.: Binary nucleation of water-sulfuric acid system: Comparison of classical theories with different  $\text{H}_2\text{SO}_4$  saturation vapor pressure, *J. Chem. Phys.*, 93, 696–701, 1990. [11544](#)
- Kulmala, M., Laaksonen, A., and Pirjola, L.: Parameterizations for sulfuric acid/water nucleation rates, *J. Geophys. Res.*, 103, 8301–8307, 1998. [11544](#)
- Laaksonen, A. and Kulmala, M.: Homogeneous heteromolecular nucleation of sulphuric acid and water vapours in stratospheric conditions: A theoretical study of the effect of hydrate interaction, *J. Aerosol Sci.*, 22, 779–787, 1991. [11544](#)
- Liu, X., Hegg, D. A., and Stoelinga, M. T.: Numerical simulation of new particle formation over northwest Atlantic using MM5 mesoscale model coupled with sulfur chemistry, *J. Geophys. Res.*, 106, 9697–9715, 2001. [11520](#), [11544](#)
- Napari, I., Noppel, M., Vehkamäki, H., and Kulmala, M.: An improved model for ternary nucleation of sulfuric acid-ammonia-water, *J. Chem. Phys.*, 116, 4221–4227, 2002a. [11520](#)
- Napari, I., Noppel, M., Vehkamäki, H., and Kulmala, M.: Parametrization of ternary nucleation rates for  $\text{H}_2\text{SO}_4\text{-NH}_3\text{-H}_2\text{O}$  vapors, *J. Geophys. Res.*, 107, doi:10.1029/2002JD002132, 2002b. [11520](#), [11521](#), [11538](#), [11544](#)
- Seinfeld, J. H. and Pandis, S. N.: *Atmospheric Chemistry and Physics, From Air Pollution to Climate Change*, John Wiley & Sons, Inc., 1998. [11544](#)

## Burst modelling

O. Hellmuth

[Title Page](#)

[Abstract](#)

[Introduction](#)

[Conclusions](#)

[References](#)

[Tables](#)

[Figures](#)

◀

▶

◀

▶

[Back](#)

[Close](#)

[Full Screen / Esc](#)

[Print Version](#)

[Interactive Discussion](#)

EGU

Stauffer, D.: Kinetic theory of two-component (“heteromolecular”) nucleation and condensation, J. Aerosol Sci., 7, 319–333, 1976. [11544](#)

Verver, G. H. I., van Dop, H., and Holtslag, A. A. M.: Turbulent mixing of reactive gases in the convective boundary layer, Boundary-Layer Meteor., 85, 197–222, 1997. [11519](#), [11520](#)

5, 11517–11555, 2005

---

## Burst modelling

O. Hellmuth

---

[Title Page](#)

[Abstract](#)

[Introduction](#)

[Conclusions](#)

[References](#)

[Tables](#)

[Figures](#)

◀

▶

◀

▶

[Back](#)

[Close](#)

[Full Screen / Esc](#)

[Print Version](#)

[Interactive Discussion](#)

EGU

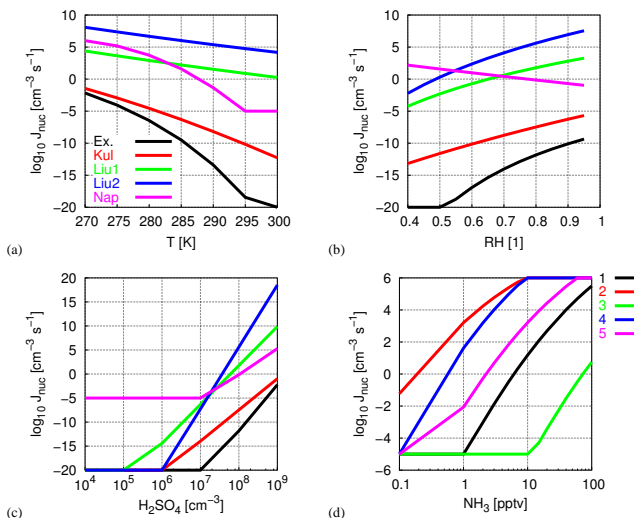


**Fig. 1.** Parameter dependence of different nucleation rate models: “Ex.” – Exact model with consideration of cluster hydration effects (Stauffer, 1976; Jaeger-Voirol et al., 1987; Jaeger-Voirol and Mirabel, 1988, 1989; Kulmala and Laaksonen, 1990; Kulmala et al., 1998; Laaksonen and Kulmala, 1991; Seinfeld and Pandis, 1998); “Kul” – Parameterization of binary nucleation rate inclusive hydration effects according to Kulmala et al. (1998); “Liu1” – Parameterization of binary nucleation rate according to Liu et al. (2001, Eq. (3)); “Liu2” – Parameterization of ternary nucleation rate at an implicate ammonia concentration of 0.5 pptv according to Liu et al. (2001, Eq. (21)); “Nap” – Parameterization of ternary nucleation rate according to Napari et al. (2002b); **(a)** Temperature dependence at  $RH=0.8$ ,  $[H_2SO_4]=10^8 \text{ cm}^{-3}$ ,  $[NH_3]=0.5 \text{ pptv}$ ; **(b)** Humidity dependence at  $T=288.15 \text{ K}$ ,  $[H_2SO_4]=10^8 \text{ cm}^{-3}$ ,  $[NH_3]=0.5 \text{ pptv}$ ; **(c)** Sulfuric acid vapour dependence at  $T=288.15 \text{ K}$ ,  $RH=0.8$ ,  $[NH_3]=0.5 \text{ pptv}$ ; **(d)** Gas-phase ammonia dependence of the ternary nucleation rate according to Napari et al. (2002b, “Nap”) for different parameter combinations of temperature, relative humidity, and sulfuric acid vapour concentration (1:  $T=288.15 \text{ K}$ ,  $RH=0.8$ ,  $[H_2SO_4]=10^7 \text{ cm}^{-3}$ ; 2:  $T=273.15 \text{ K}$ ,  $RH=0.8$ ,  $[H_2SO_4]=10^7 \text{ cm}^{-3}$ ; 3:  $T=288.15 \text{ K}$ ,  $RH=0.8$ ,  $[H_2SO_4]=10^6 \text{ cm}^{-3}$ ; 4:  $T=288.15 \text{ K}$ ,  $RH=0.8$ ,  $[H_2SO_4]=10^8 \text{ cm}^{-3}$ ; 5:  $T=288.15 \text{ K}$ ,  $RH=0.4$ ,  $[H_2SO_4]=10^7 \text{ cm}^{-3}$ ). **11544**

## Burst modelling

O. Hellmuth

[Title Page](#)

[Abstract](#)

[Introduction](#)

[Conclusions](#)

[References](#)

[Tables](#)

[Figures](#)

◀

▶

◀

▶

[Back](#)

[Close](#)

[Full Screen / Esc](#)

[Print Version](#)

[Interactive Discussion](#)

EGU

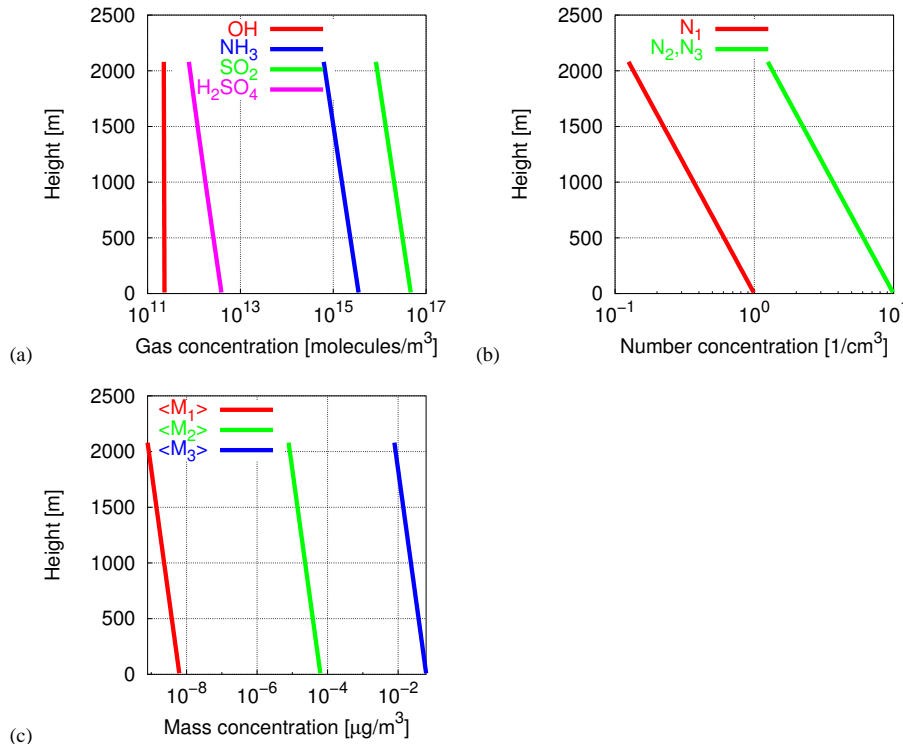


**Fig. 2.** Initial vertical profiles: **(a)** Gas-phase concentration; **(b)** Number concentration; **(c)** Mass concentration.

## Burst modelling

O. Hellmuth

[Title Page](#)

[Abstract](#)

[Introduction](#)

[Conclusions](#)

[References](#)

[Tables](#)

[Figures](#)

[|◀](#)

[▶|](#)

[◀](#)

[▶](#)

[Back](#)

[Close](#)

[Full Screen / Esc](#)

[Print Version](#)

[Interactive Discussion](#)

EGU

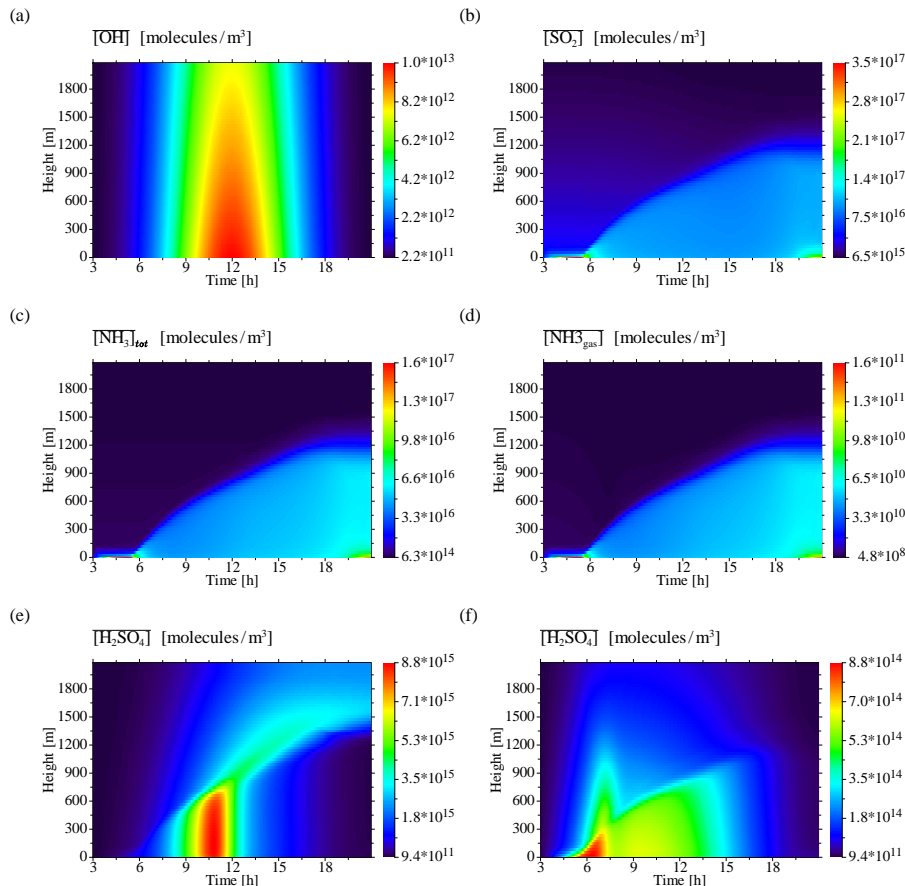


**Fig. 3.** First-order moments of physico-chemical variables: (a) Hydroxyl radical; (b) Sulfur dioxide; (c) Total ammonia; (d) Gas phase ammonia; (e) Sulfuric acid – binary case; (f) Sulfuric acid – ternary case.

## Burst modelling

O. Hellmuth

[Title Page](#)

[Abstract](#)

[Introduction](#)

[Conclusions](#)

[References](#)

[Tables](#)

[Figures](#)

◀

▶

◀

▶

[Back](#)

[Close](#)

[Full Screen / Esc](#)

[Print Version](#)

[Interactive Discussion](#)

EGU

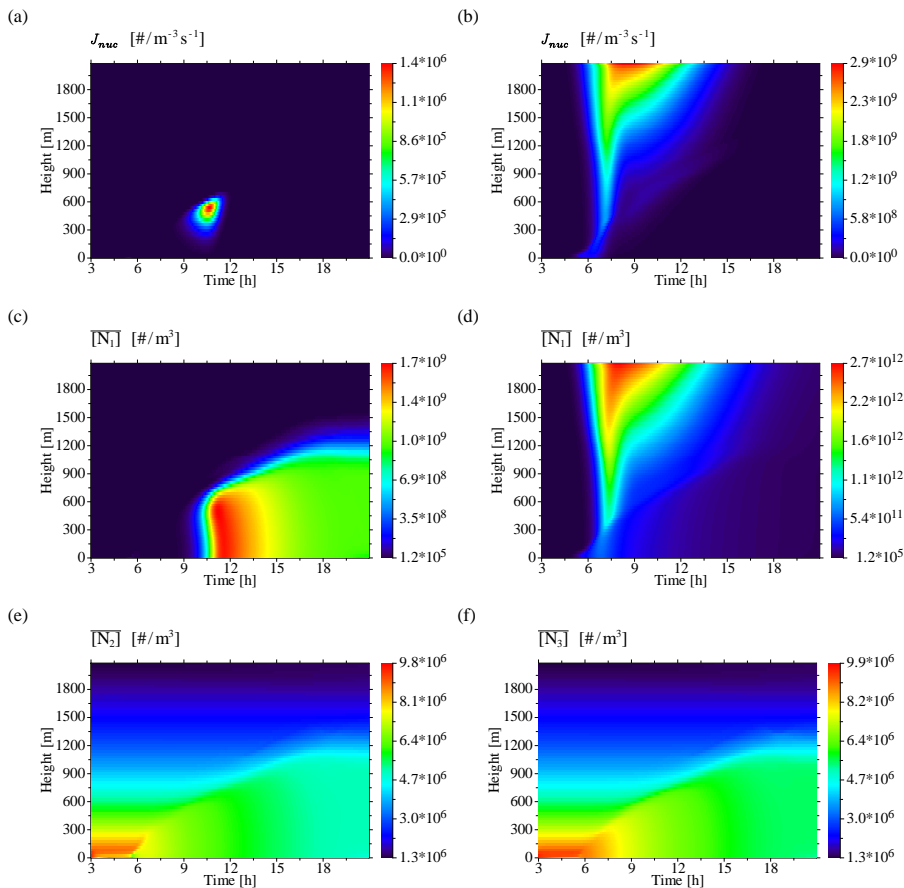


**Fig. 4.** First-order moments of physico-chemical variables: **(a)** Binary nucleation rate; **(b)** Ternary nucleation rate; **(c)** UCN number concentration – binary case; **(d)** UCN number concentration – ternary case; **(e)** Aitken mode number concentration – binary case; **(f)** Accumulation mode number concentration – binary case.

[Title Page](#)[Abstract](#)[Introduction](#)[Conclusions](#)[References](#)[Tables](#)[Figures](#)[◀](#)[▶](#)[◀](#)[▶](#)[Back](#)[Close](#)[Full Screen / Esc](#)[Print Version](#)[Interactive Discussion](#)

## Burst modelling

O. Hellmuth

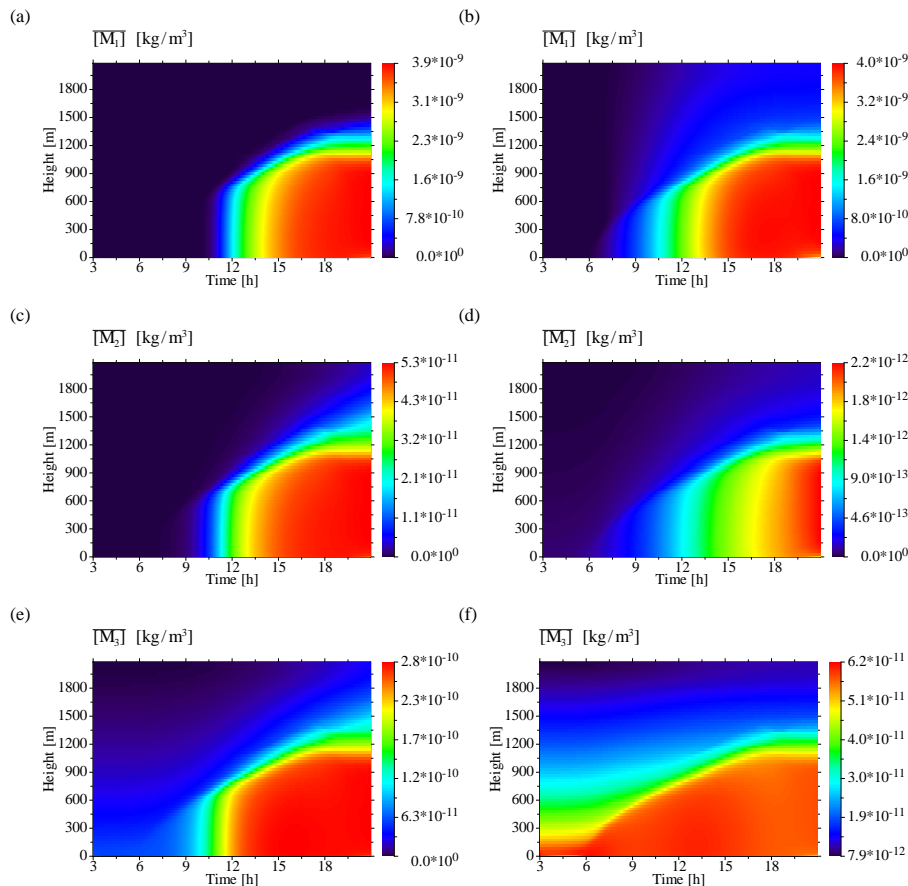


**Fig. 5.** First-order moments of physico-chemical variables: **(a)** UCN mass concentration – binary case; **(b)** UCN mass concentration – ternary case; **(c)** Aitken mode mass concentration – binary case; **(d)** Aitken mode mass concentration – ternary case; **(e)** Accumulation mode mass concentration – binary case; **(f)** Accumulation mode mass concentration – ternary case.

<a href="#">Title Page</a>	
<a href="#">Abstract</a>	<a href="#">Introduction</a>
<a href="#">Conclusions</a>	<a href="#">References</a>
<a href="#">Tables</a>	<a href="#">Figures</a>
<a href="#"></a>	<a href="#"></a>
<a href="#"></a>	<a href="#"></a>
<a href="#">Full Screen / Esc</a>	
<a href="#">Print Version</a>	
<a href="#">Interactive Discussion</a>	

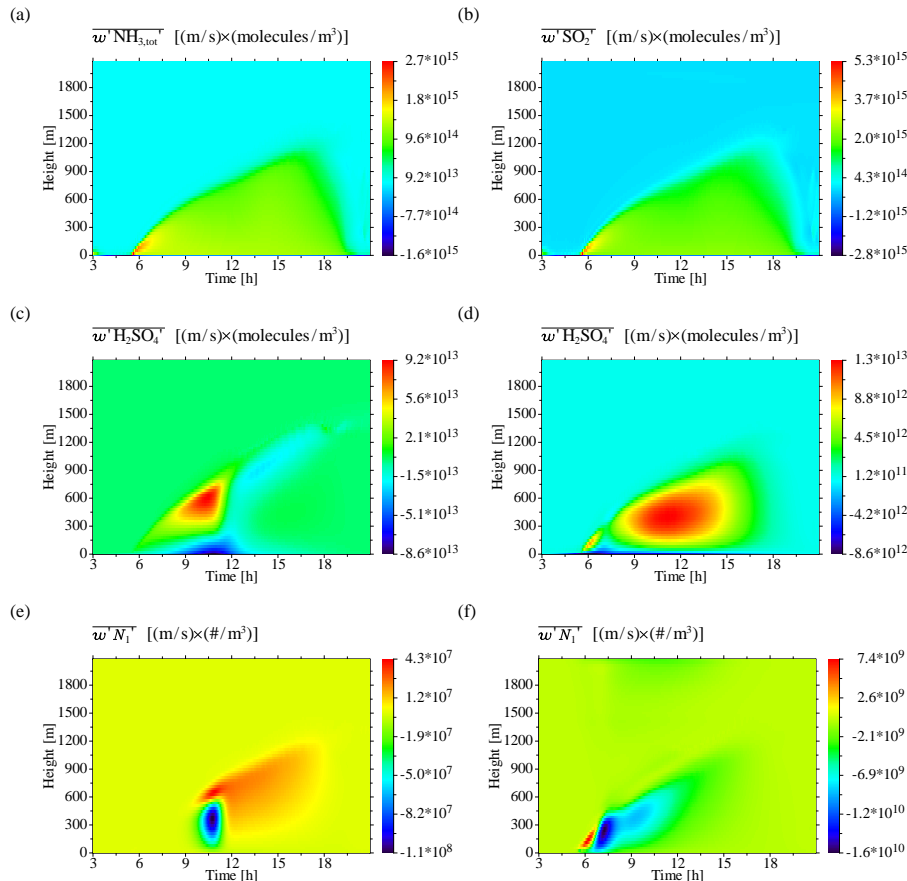


**Fig. 6.** Turbulent vertical fluxes of physico-chemical species: (a) Total ammonia flux; (b) Sulfur dioxide flux; (c) Sulfuric acid flux – binary case; (d) Sulfuric acid flux – ternary case; (e) UCN number concentration flux – binary case; (f) UCN number concentration flux – ternary case.

## Burst modelling

O. Hellmuth

[Title Page](#)

[Abstract](#)

[Introduction](#)

[Conclusions](#)

[References](#)

[Tables](#)

[Figures](#)

◀

▶

◀

▶

[Back](#)

[Close](#)

[Full Screen / Esc](#)

[Print Version](#)

[Interactive Discussion](#)

EGU

## Burst modelling

O. Hellmuth

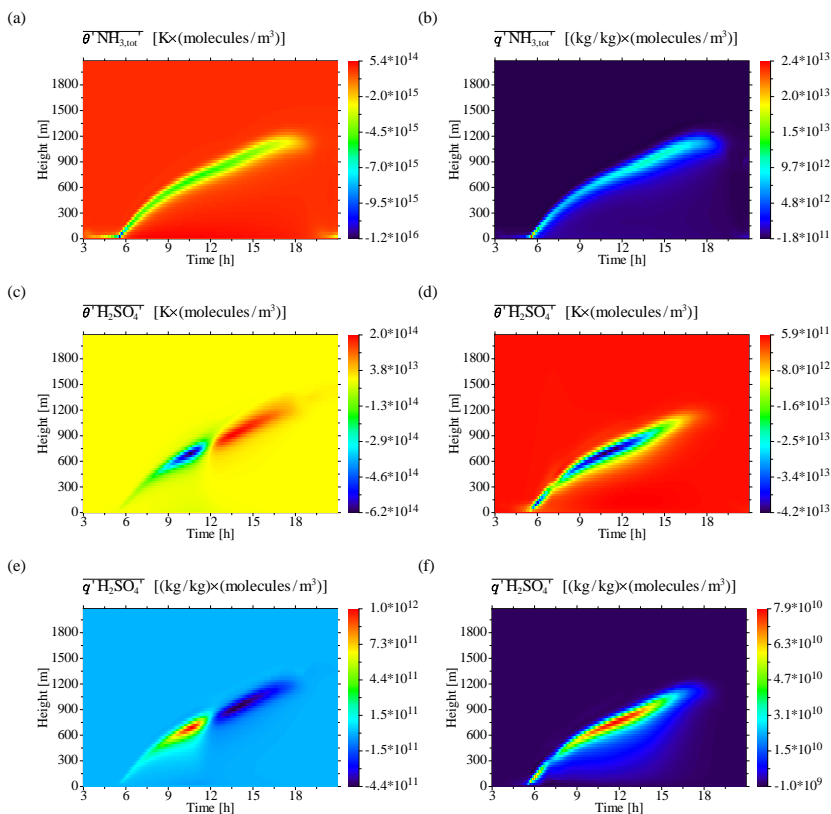


**Fig. 7.** Covariances of meteorological parameters and physico-chemical properties: (a) Covariance of potential temperature and total ammonia concentration; (b) Covariance of water vapour mixing ratio and total ammonia concentration; (c) Covariance of potential temperature and sulfuric acid concentration – binary case; (d) Covariance of potential temperature and sulfuric acid concentration – ternary case; (e) Covariance of water vapour mixing ratio and sulfuric acid concentration – binary case; (f) Covariance of water vapour mixing ratio and sulfuric acid concentration – ternary case.

[Title Page](#)[Abstract](#)[Introduction](#)[Conclusions](#)[References](#)[Tables](#)[Figures](#)[◀](#)[▶](#)[◀](#)[▶](#)[Back](#)[Close](#)[Full Screen / Esc](#)[Print Version](#)[Interactive Discussion](#)

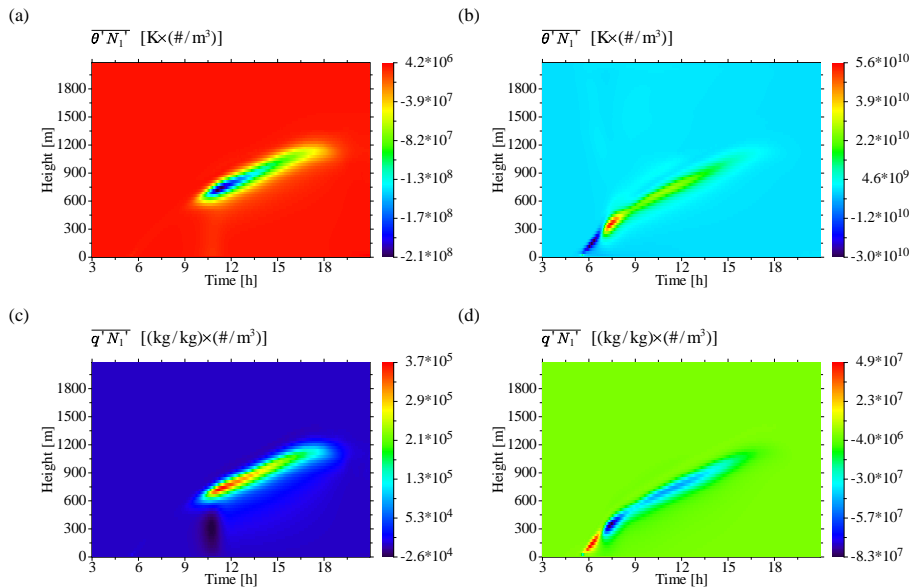


**Fig. 8.** Covariances of meteorological parameters and physico-chemical properties: **(a)** Covariance of potential temperature and UCN number concentration – binary case; **(b)** Covariance of potential temperature and UCN number concentration – ternary case; **(c)** Covariance of water vapour mixing ratio and UCN number concentration – binary case; **(d)** Covariance of water vapour mixing ratio and UCN number concentration – ternary case.

## Burst modelling

O. Hellmuth

[Title Page](#)

[Abstract](#)

[Introduction](#)

[Conclusions](#)

[References](#)

[Tables](#)

[Figures](#)

[◀](#)

[▶](#)

[◀](#)

[▶](#)

[Back](#)

[Close](#)

[Full Screen / Esc](#)

[Print Version](#)

[Interactive Discussion](#)

EGU

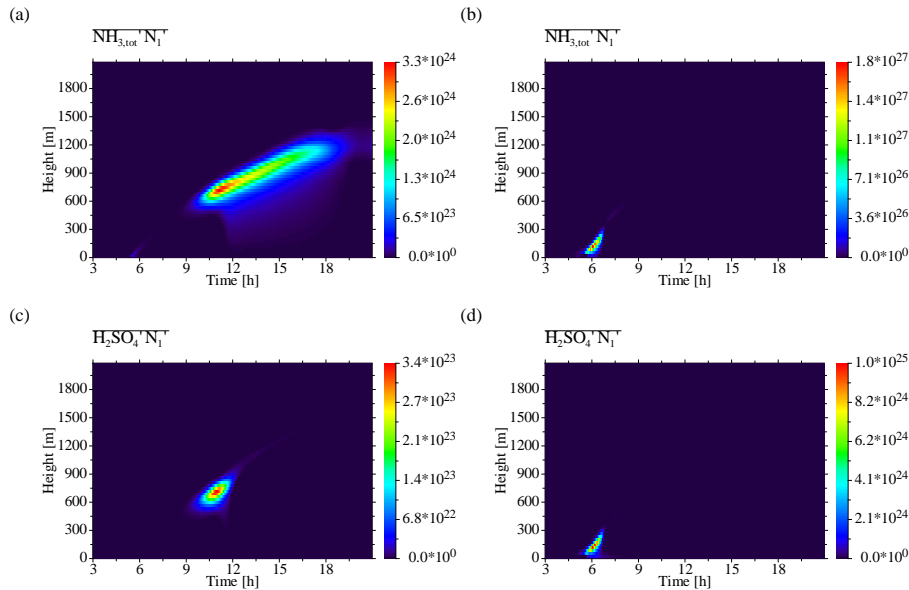


**Fig. 9.** Covariances of gas-phase concentrations and UCN number concentration: **(a)** Covariance of total ammonia concentration and UCN number concentration – binary case; **(b)** Covariance of total ammonia concentration and UCN number concentration – ternary case; **(c)** Covariance of sulfuric acid concentration and UCN number concentration – binary case; **(d)** Covariance of sulfuric acid concentration and UCN number concentration – ternary case.

## Burst modelling

O. Hellmuth

[Title Page](#)

[Abstract](#)

[Introduction](#)

[Conclusions](#)

[References](#)

[Tables](#)

[Figures](#)

◀

▶

◀

▶

[Back](#)

[Close](#)

[Full Screen / Esc](#)

[Print Version](#)

[Interactive Discussion](#)

EGU

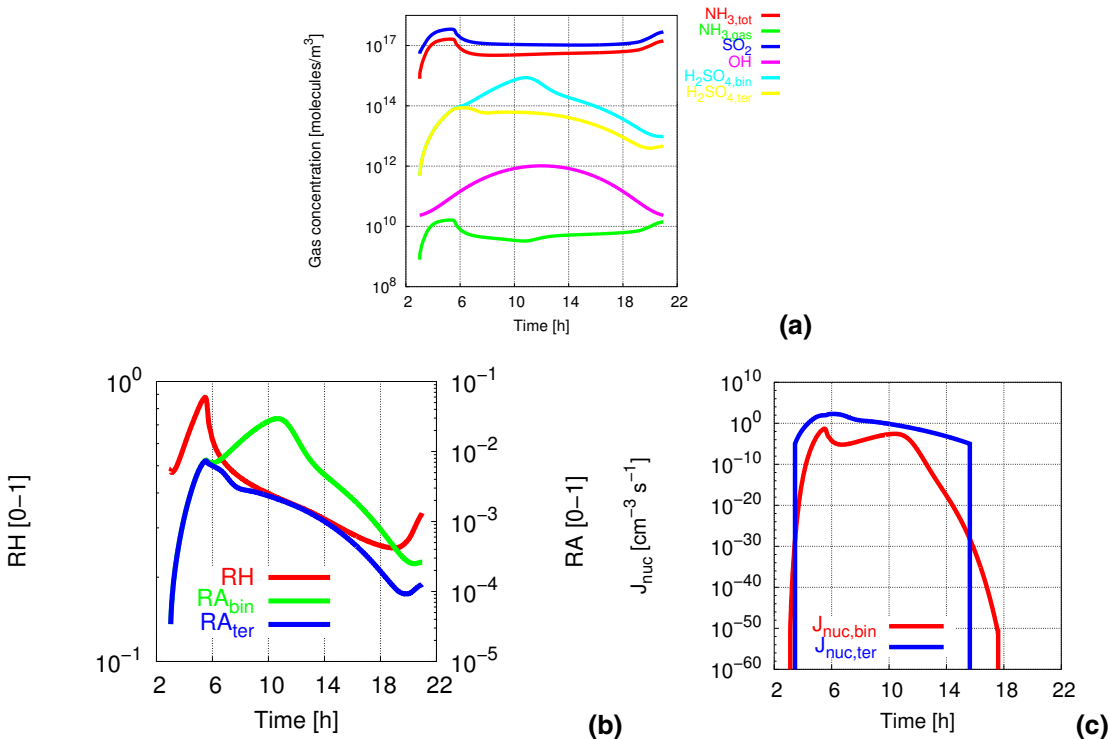


**Fig. 10.** Time series of physico-chemical properties in the Prandtl layer: **(a)** Gas-phase species; **(b)** Relative humidity and relative acidity; **(c)** Nucleation rate.

## Burst modelling

O. Hellmuth

[Title Page](#)

[Abstract](#)

[Introduction](#)

[Conclusions](#)

[References](#)

[Tables](#)

[Figures](#)

[◀](#)

[▶](#)

[◀](#)

[▶](#)

[Back](#)

[Close](#)

[Full Screen / Esc](#)

[Print Version](#)

[Interactive Discussion](#)

EGU

## Burst modelling

O. Hellmuth

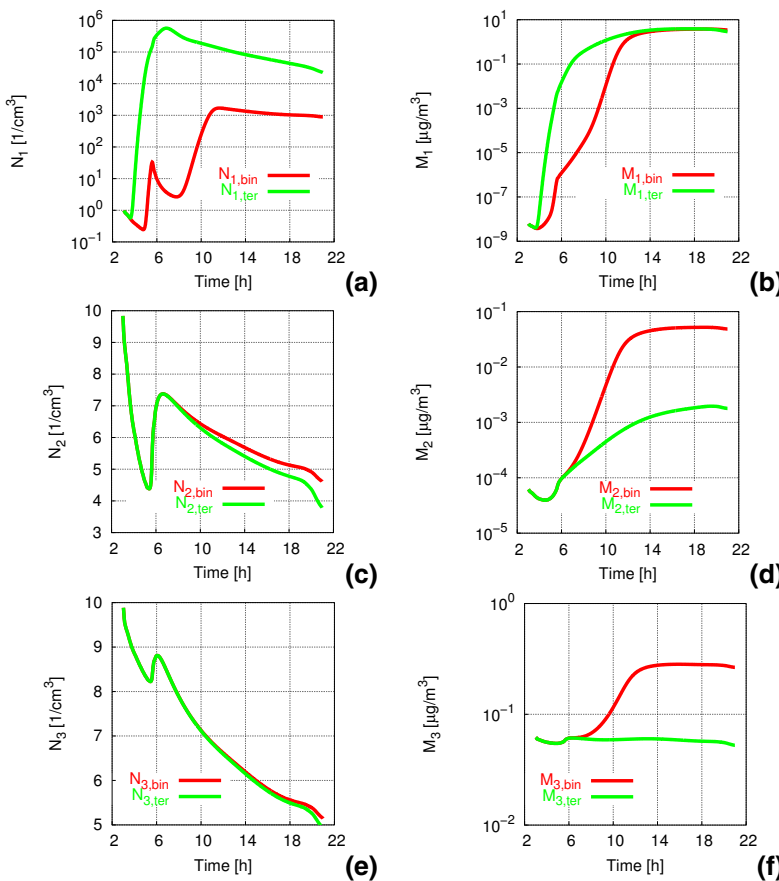


**Fig. 11.** Time series of physico-chemical properties in the Prandtl layer: **(a)** Nucleation mode: Number concentration; **(b)** Nucleation mode: Mass concentration; **(c)** Aitken mode: Number concentration; **(d)** Aitken mode: Mass concentration; **(e)** Accumulation mode: Number concentration; **(f)** Accumulation mode: Mass concentration.

[Title Page](#)[Abstract](#)[Introduction](#)[Conclusions](#)[References](#)[Tables](#)[Figures](#)[◀](#)[▶](#)[◀](#)[▶](#)[Back](#)[Close](#)[Full Screen / Esc](#)[Print Version](#)[Interactive Discussion](#)

**Burst modelling**

O. Hellmuth

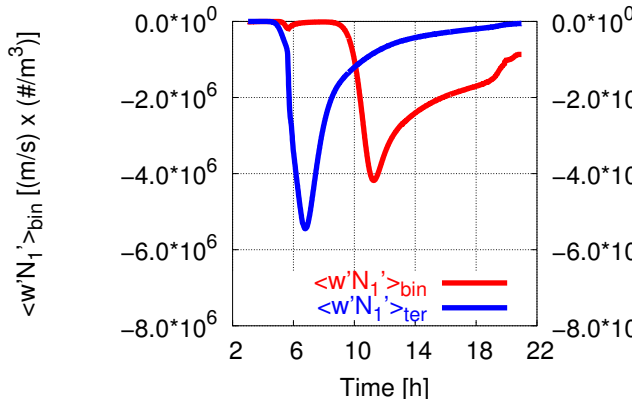


**Fig. 12.** Time series of physico-chemical properties in the Prandtl layer: Turbulent vertical flux of UCN nuclei for binary and ternary nucleation.

[Title Page](#)[Abstract](#)[Introduction](#)[Conclusions](#)[References](#)[Tables](#)[Figures](#)[◀](#)[▶](#)[◀](#)[▶](#)[Back](#)[Close](#)[Full Screen / Esc](#)[Print Version](#)[Interactive Discussion](#)

EGU